Human Brain Mapping

WILEY

RESEARCH ARTICLE OPEN ACCESS

Relationships Between Intra-Spinal Resting-State Functional Connectivity and Electrophysiology Following Spinal Cord Injury

Pai-Feng Yang[1,2] | Jamie L. Reed[1,2] | Anirban Sengupta[1,2] | Arabinda Mishra[1,2] | Feng Wang[1,2] | John C. Gore[1,2,3] | Li Min Chen[1,2,3]

[1]Institute of Imaging Science, Vanderbilt University, Nashville, Tennessee, USA | [2]Department of Radiology and Radiological Sciences, Vanderbilt University Medical Center, Nashville, Tennessee, USA | [3]Biomedical Engineering, Vanderbilt University, Nashville, Tennessee, USA

Correspondence: Li Min Chen (limin.chen@vanderbilt.edu)

Received: 5 May 2025 | **Revised:** 26 August 2025 | **Accepted:** 19 September 2025

Funding: This work was supported by National Institutes of Health (2R01NS078680).

Keywords: fMRI | local field potential | non-human primates | resting state functional connectivity | spinal cord injury

ABSTRACT

We previously reported that a unilateral dorsal column lesion (DCL) at the cervical C4 level primarily reduces inter-horn resting-state functional connectivity (rsFC) measured by functional Magnetic Resonance Imaging (fMRI) in segments below the lesion. This study compares changes in rsFC from fMRI with changes in local field potential (LFP) coherence over an extended post-injury period. High-resolution fMRI and LFP data were acquired bilaterally in healthy monkeys and at 3- and 6-months post-lesion. At 3 months post-injury, tactile-stimulus-evoked LFP power in the dorsal horn was significantly weaker than in the healthy cord and non-lesion side. LFP coherences increased on the lesion side for the dorsal-to-intermediate zone (D-IGM) and dorsal-to-ventral (D-V) pairs but decreased for the non-lesion side D-IGM. By 6 months, stimulus-evoked LFP power on the lesion side remained low. LFP coherences between dorsal-to-dorsal (D-D), ventral-to-ventral (V-V), and D-V pairs on both the lesion and non-lesion sides were significantly reduced relative to the healthy cord. Low-frequency (delta, theta, and alpha) D-IGM coherences on the lesion side, and high-frequency (beta and gamma) coherences on the non-lesion side, were also significantly weakened. Across specific inter-horn pairs and time points, changes in LFP coherences and rsFC measures were weakly correlated. Measurements of inter-horn correlations two segments caudal to the lesion level at C7 revealed distance-dependent intraspinal connectivity changes following DCL. Post-mortem histology confirmed a complete DCL in most animals (7/9). The extent of the disruption of ascending sensory afferents, as assessed histologically, did not appear to correlate with the degree of LFP power reduction or rsFC changes at post-injury time points. In summary, we observed temporally and spatially heterogeneous changes of fMRI correlations and LFP coherences within intraspinal circuits. fMRI rsFC and LFP coherences were not always concordant, with discrepancies depending on specific gray-matter horns and intermediate-zone pairs.

1 | Introduction

The spinal cord is a processing and relay center between the body and the brain, and its proper function is essential for transmitting and integrating sensory and motor information as well as controlling autonomic functions. Injury to the spinal cord leads to catastrophic functional and behavioral impairments. To date, the successful development of effective therapeutic interventions

John C. Gore and Li Min Chen contributed equally to this study.

This is an open access article under the terms of the Creative Commons Attribution-NonCommercial-NoDerivs License, which permits use and distribution in any medium, provided the original work is properly cited, the use is non-commercial and no modifications or adaptations are made.

© 2025 The Author(s). *Human Brain Mapping* published by Wiley Periodicals LLC.

has been constrained by a lack of tools that provide objective assessments of the injury progression and recovery, which can be used for clinical trials that promote recovery following spinal cord injury (SCI). Our group pioneered the use of fMRI to assess the function and integrity of intraspinal circuits and found that resting-state functional connectivity (rsFC) measures between spinal cord gray matter zones are sensitive and specific biomarkers of the functional status and circuit integrity across species from rodents to nonhuman primates and to humans (Barry et al. 2018; Barry et al. 2016; Chen et al. 2015; Combes et al. 2023; Combes et al. 2022; Kinany et al. 2020, 2023; Kong et al. 2014; Wu et al. 2018). We have identified strong rsFC between gray matter horns within and across healthy spinal segments (Chen et al. 2015; Sengupta et al. 2021; Wu et al. 2018). A unilateral dorsal column lesion (DCL) at cervical spinal cord segment 5 (C5) in squirrel monkeys disrupts rsFC between gray matter signals on the side of injury and in segments below the injury (Chen et al. 2015). These patterns of rsFC disruptions of the intraspinal circuits, particularly in spinal segments below the SCI level, correlated with the severity of behavioral deficits and extent of recovery, supporting their roles as non-invasive imaging biomarkers.

Given the hemodynamic nature of MRI signals as indirect indicators of neural activity, it is crucial to understand the extent to which changes in rsFC reflect neuronal functional connectivity changes within the spinal cord, and how they correspond before and after injury. A clear confirmation of the neural basis of rsFC at rest, as well as fMRI signal changes during the processing of tactile inputs in the spinal cord, is essential for the proper interpretation of fMRI observations and their applications. Previously, we demonstrated that coherence between local field potentials (LFPs) measured between pairs of electrodes in multi-electrode arrays showed spatial (depth) and temporal patterns similar to BOLD-based measurements of rsFC in healthy spinal cord (Wu et al. 2019). In the present study, using a unilateral DCL model, we aimed to: (a) measure the effects of DCL on LFP signals recorded from the segment immediately below the lesion in cervical spinal cord; (b) establish the relationships between fMRI and LFP signals by comparing temporal changes in LFP functional connectivity with changes in fMRI rsFC; and (c) interpret LFP power changes by relating them to the extent of spinal cord lesions assessed via post-mortem histology. While our long-term goal is to validate resting-state fMRI (rsfMRI) rsFC as a surrogate of neural functional connectivity and a biomarker of circuit-level integrity in the cervical spinal cord of non-human primates, in this study, we focused on the temporal relationship between post-SCI changes in rsFC and LFP coherence following a traumatic unilateral DCL. Because LFP signals are commonly analyzed across distinct frequency bands that may represent specific aspects of neurophysiological processes, we examined the temporal dynamics of broadband and five specific LFP frequency bands at 3- and 6 months post-injury and compared these findings with functional connectivity measured by fMRI.

2 | Materials and Methods

2.1 | General Information

A total of 13 adult male squirrel monkeys (*Saimiri sciureus*) were included in this study. Nine monkeys received spinal cord injuries, and two of these underwent spinal cord electrophysiology recordings around 3 months post-injury, while the other seven underwent spinal cord recordings around 6 months post-injury. Four monkeys that did not undergo spinal cord injury procedures were used as normal controls. Six out of the 9 DCL monkeys were scanned before and multiple times (post-lesion at week 1, 2, 4, 6, 8, 13, 16, 20, 24, 32) after DCL. Microelectrode electrophysiology recordings were performed after the completion of MRI data acquisition, during which time, animals are expected to show significant recovery of impaired hand use (Qi et al. 2016; Wang et al. 2018). A comprehensive data acquisition timeline for each animal is summarized in Table S1.

2.2 | Animal Preparation

Each animal was initially sedated with ketamine hydrochloride (10 mg/kg, IM), given atropine (0.05 mg/kg, IM), intubated, and then anesthetized with isoflurane (0.8%–1.2%) delivered in a 30:70 O_2:N_2O mixture. Animals were artificially ventilated to maintain an end-tidal CO_2 of 4%, while the head and body were stabilized in an MR-compatible frame for imaging or a stereotaxic frame for electrophysiology. Rectal temperature was monitored, and a water-circulating heating pad was used to maintain the body core temperature at 37.5°C–38.5°C. Vital signs, including SpO_2, heart rate, and respiration pattern, were continuously monitored and recorded. Recorded respiration signals were later used in fMRI data processing. Intravenous administration of saline or 2.5% dextrose in lactated Ringer's solution (3 mL/kg/h) was given throughout the procedure to prevent dehydration and provide caloric energy. All procedures followed NIH guidelines and were approved by the Institutional Animal Care and Use Committee of Vanderbilt University (IACUC # M1600079; initial approval date: April 2016, latest renewal approval date: April 2025). Vanderbilt University is an AAALAC-accredited institution for animal research.

2.3 | Spinal Cord Injury Model—Unilateral DCL

The dorsal portion of the lower cervical spinal cord at the C4-C6 level was exposed under surgical levels of anesthesia and aseptic conditions. The dorsal column pathway (tract) was transected on the dominant hand side with a pair of fine surgical scissors at the level between the C4 and C5 segments. Each lesion was 2 mm deep and ran from the midline to the spinal nerve entry zone (~2 mm in width). Dura was replaced with a small piece of Gelfilm (Pfizer), and the wound was closed. Standard post-surgery care, including administration of analgesics and routine checkups by researchers and veterinary staff, was provided according to the protocol approved by the IACUC. The details of the surgical procedures can be found in previous publications (Chen et al. 2012; Qi et al. 2011, 2016).

2.4 | MRI Data Acquisition

MRI scans were conducted on an Agilent 9.4 T scanner. A customized saddle-shaped quadrature coil with two loops—each measuring $3 \times 3\,cm^2$—mounted on a cylindrical surface, was positioned over each animal's neck. Five contiguous axial

image slices (each 3 mm in thickness) covering the C3–C7 cervical segments, with the third slice positioned over the C5 segment (where the lesion was targeted), were acquired in each imaging session. For squirrel monkeys, C5–C7 are the enlarged spinal segments that receive sensory input from the upper arm and hand/digits. High-resolution ($0.25 \times 0.25\,mm^2$ in-plane resolution, 128×128 matrix) structural magnetization transfer contrast (MTC) weighted images [TR (repetition time)/TE (echo time): 220/3.24 ms] were acquired using a gaussian radio frequency (RF) saturation pulse (flip angle, 820°; pulse width, 12 ms; RF offset, 5000 Hz). FMRI imaging data were collected from the same five slices. Each rsfMRI imaging run consisted of 300 dynamics acquired using a fast gradient echo sequence (flip angle = ~18°, TR = 46.88 ms, TE: 6.5 ms, 3 s per volume) with an in-plane resolution of $0.5 \times 0.5\,mm^2$ (64×64 matrix).

The rsfMRI data were acquired from six out of the 9 DCL animals (SM1-SM6 in Table S1) before (pre-lesion, $n = 18$ runs) and after spinal cord injury at multiple time points post-lesion. 90 fMRI runs collected within 1–9 weeks and 48 runs collected within 16–32 weeks post-lesion were included in the group analysis.

2.5 | FMRI Data Preprocessing and Analysis

All resting state fMRI data underwent slice-by-slice 2D motion correction in MATLAB R2019a. Motion parameters, along with temporal signals extracted from muscle and CSF regions containing at least 70% of the cumulative variance (derived using principal components analysis), were considered nuisance parameters and regressed out using a general linear model (Barry et al. 2018; Barry et al. 2016; Chen et al. 2015; Sengupta et al. 2021; Wu et al. 2019). No spatial smoothing was performed. Physiological noise (respiratory signal) was corrected using RETROICOR (Glover et al. 2000). RsfMRI signals were band-pass filtered (Chebyshev type 2 IIR filter, cut-off frequencies 0.01 and 0.1 Hz). Each subject's MTC anatomic images were coregistered to a custom spinal cord template, and the transformation was applied to the functional fMRI data using FSL to perform a group analysis (Jenkinson and Smith 2001). This custom template was generated from the pre-injury spinal cord MTC structural images, selected for its highest gray–white matter contrast among subjects studied. The use of a custom neck coil and careful shimming helped minimize distortions and misalignment between the fMRI and MTC images. Representative alignments are shown in Figure S1. Axial fMRI images were up-sampled to the anatomic MTC image resolution for visualization. Locations of the spinal nerve afferent bundles and their spatial relationships within the spinal cord were used as landmarks to align axial images across imaging sessions of the same animal and across animals. Seven regions of interest (ROIs, bilateral dorsal horn, ventral horn, intermediate zone, and gray commissure) were identified by conducting an independent component analysis (ICA) of rsfMRI data (GIFT software; Calhoun et al. 2001) acquired from C3–C7 segments.

We performed a group-level analysis on six monkeys who received MRI scans, using the ICA-derived regions described in (Sengupta et al. 2021). These regions were obtained from a total of 16 monkeys, of whom five monkeys were included in this study and 11 who were not. The ICA model order was determined based on a combination of prior theory and literature, as well as empirical evidence from our dataset. Specifically, we selected 35 components (ROIs) across five axial slices (seven per slice).

Subsequently, rsfMRI signals were extracted from each ROI for pairwise quantification of inter-ROI Pearson correlation coefficients (r values) for all six pairs of ROIs (excluding the gray commissure) within each slice. The r value for which $p < 0.05$ (FDR corrected) was considered statistically significant.

Those inter-ROI correlations were presented as whisker box plots at different time points, including pre-injury (pre-SC), 1–9 weeks (post-SCI 1), and 16–32 weeks post-injury (post-SCI 2). Before statistical analysis, we conducted Bartlett's test to assess the assumption of equal variances and determine variance heterogeneity on both fMRI and LFP data, and determined that the Brown-Forsythe ANOVA test is appropriate. Different ROI pairs were compared using a Brown-Forsythe ANOVA test, followed by a Dunnett test for pairwise comparisons, for which $p < 0.05$ was considered statistically significant.

Electrophysiology and fMRI data were not acquired in the same sessions to protect MRI image quality and to avoid artifacts related to surgery, laminectomy, and electrode implantation. Because fMRI sessions were more frequent than electrophysiology, we binned fMRI data into two windows (1–9 and 16–32 weeks) to align with the electrophysiology time points at approximately 3 and 6 months post-lesion. It is noted that the transverse diameter of the cervical enlargement segments of squirrel monkeys averages 6.5 mm (range, 6–7 mm). This corresponds to approximately 12–14 voxels across the left–right axis.

2.6 | Electrophysiology Data Acquisition and Analysis

LFP signals were obtained from the spinal cord on both sides within one segment below the lesion level, typically in segment C5. For electrophysiology recordings, we implemented two steps to minimize spinal cord movements associated with cardiac and respiration cycles. First, we stabilized the spinal cord by lifting the C7 vertebra away from the chest with clamps to reduce respiration-related motion. Second, we applied 4% agarose to the exposed spinal cord, which substantially reduced cardiac-cycle–related movement. We examined LFP power spectra to identify physiologic artifacts and to verify the effectiveness of these measures.

We mapped digit representations on both sides of the spinal cord dorsal horn to determine target locations for linear array recording. We manually palpated the hands and digits to locate the regions that contain neurons with receptive fields on the hand and digits. Two 16-channel linear arrays (Microprobes for Life Science) with 150 μm contact spacing were placed on both sides of the spinal cord. Spiking and LFP signals were recorded with multi-channel digital acquisitions (CerePlex Direct, BlackRock

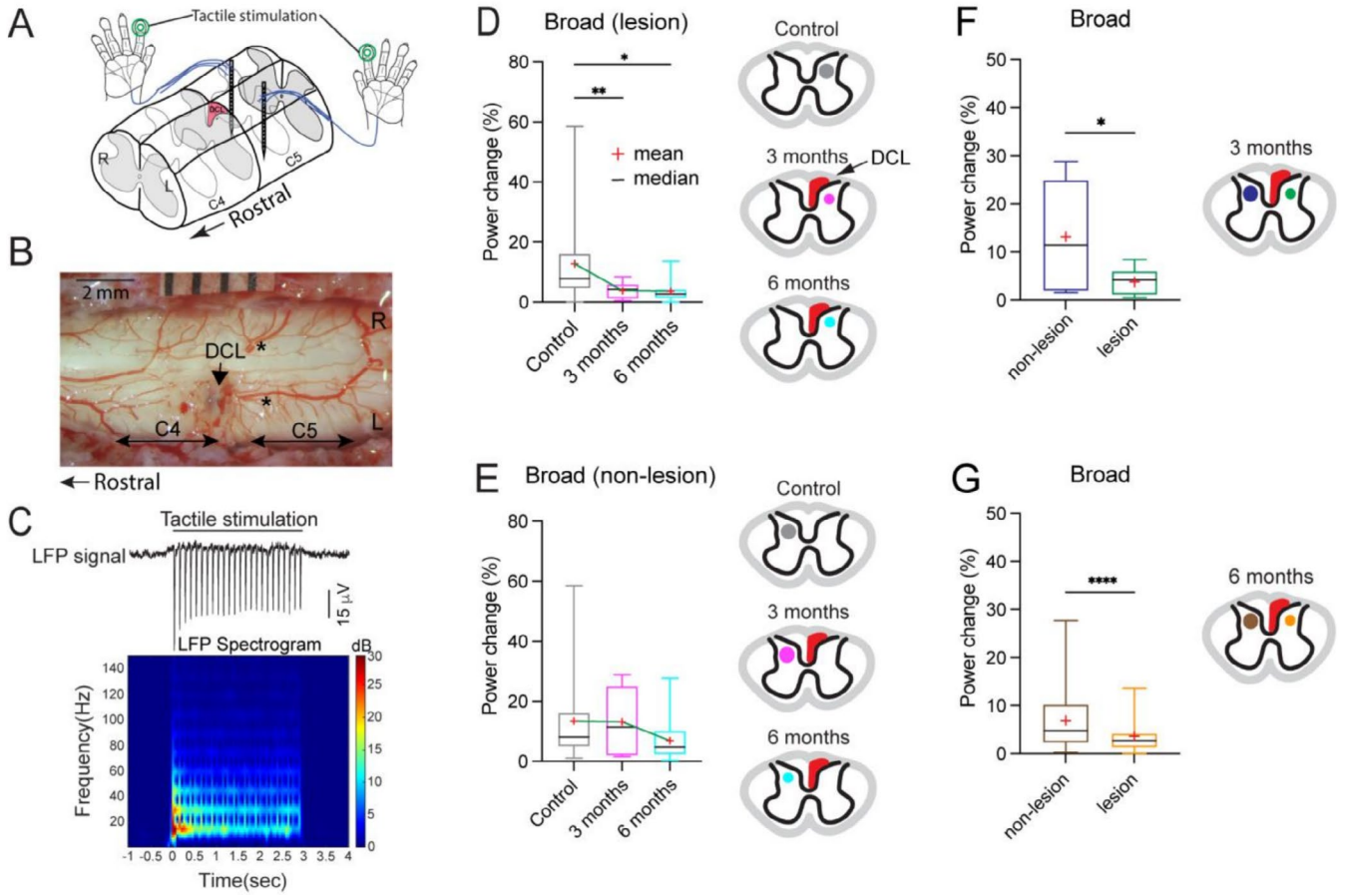

FIGURE 1 | Temporal dynamics of vibrotactile stimulus-evoked LFP power following dorsal column lesion (DCL) below the lesion level. (A) Schematic illustration of LFP recordings from bilateral spinal cord gray matter using two linear electrode arrays. (B) Photograph of the exposed spinal cord showing the DCL and recording sites (black asterisks). (C) Examples of 8 Hz tactile stimulus-evoked increases in LFP signal amplitude (top panel) and corresponding time-frequency spectra (bottom panel). (D, E) Box plots showing changes in broadband stimulus-evoked LFP power in healthy controls ($n = 4$ monkeys), and at 3 months ($n = 2$) and 6 months ($n = 6$) post-DCL on the lesion side (D) and non-lesion side (E). (F, G) Box plots comparing broadband LFP power changes between lesion and non-lesion sides at 3 months (F) and 6 months (G) post-injury. Statistical analyses were conducted using Brown-Forsythe ANOVA with a Dunnett test. (D and E) or unpaired *t*-tests (F, G). Significance levels: $^{*}p < 0.05$, $^{**}p < 0.005$, $^{****}p < 0.0001$. The median and mean are indicated by horizontal lines and red plus symbols, respectively, in each box plot. Smaller colored dots represent reduced LFP power changes in response to fingertip tactile stimulation.

Microsystems). Both LFP and spiking activity were acquired in a resting state and during 8 Hz vibrotactile digit stimulation conditions. LFP signals were sampled at 1 kHz and then band-pass filtered between 1 and 150 Hz using a second-order, zero-phase Chebyshev 1 band-pass filter. A 60 Hz notch filter was also used to remove electrical power frequency interference during data preprocessing. Signal preprocessing and analysis were conducted using the FieldTrip toolbox in MATLAB (Oostenveld et al. 2011).

The same six ROIs (bilateral dorsal and ventral horns and intermediate zones) used in fMRI data analysis were identified for quantification as follows. The electrode contact that showed the strongest LFP amplitude increase in response to tactile stimulation of fingers was identified as the contact at spinal Rexed lamina IV within the dorsal horn. Based on the MRI image-derived gray matter structure and size and known electrode contact spacing (150 μm), we estimated that the electrode contacts within the intermediate zone are about 800–1200 μm from the dorsal lamina IV responsive zone. Contacts at least 500 μm away from the intermediate zone contacts were assigned to be contacts within the ventral horn. These measures are similar to estimates of compartments of the cervical spinal gray matter in squirrel monkeys according to high-field MRI images (Wu et al. 2019). Figure 1 provides methodological schematics.

LFP signals were collected during both tactile stimulation and resting states. For stimulation trials, an 8 Hz vibrotactile stimulus (pulse duration: 20 ms) was repeatedly applied to a single distal fingerpad for 3 s per stimulus epoch. Within each trial, the stimulus epoch was repeated 30–50 times, with 5-s intervals between repetitions. Typically, 3–13 trials were collected for each monkey. Percentages of LFP power changes were calculated for the broadband range (1–150 Hz) and the following frequency bands: delta (1–4 Hz), theta (5–8 Hz), alpha (9–14 Hz), beta (15–30 Hz), and low gamma band (30–80 Hz). We conducted the Brown-Forsythe ANOVA test, followed by a Dunnett test for pairwise comparisons among three groups: 'control,' '3 months,' and '6 months.' In cases where 3 months post-DCL data were unavailable, unpaired t-tests were used to assess differences between two conditions. The significance level was set at alpha = 0.05.

For resting-state LFP recordings, 6–10 trials of resting-state LFP signals, each lasting 10–15 min, were collected in each monkey. Resting-state LFP signals were de-noised by notch-filtering the first five harmonics of the respiration frequency. Magnitude-squared coherence—a function of the power and cross-power spectral densities between two signals—was computed between LFP signals recorded from pairs of gray matter regions, including dorsal-to-dorsal horns (D-D); ventral-to-ventral horns (V-V); dorsal-to-ventral horns (D-V); dorsal-to-intermediate gray matter (D-IGM). Inter-regional LFP coherence was used to quantify the functional connectivity between spinal cord regions. To characterize the temporal relationship between changes in LFP and rsFC over time, we employed both correlation analysis and power law fitting.

2.7 | Histological Validation of Injury

Before the final experimental session, transganglionic transport tracer cholera toxin subunit B (CTB, Sigma, 1% in phosphate-buffered saline) was injected into the distal digits 1, 3, and 5 of both hands in each animal. The tracer injections were detected in both lesioned and non-lesioned sides of the spinal cord and brainstem. Then, quantification of the difference between the labeling of axon terminals in the cuneate nucleus was used to indicate the extent of the lesion that blocked axons from transporting CTB from the spinal cord to the brainstem (Qi et al. 2011). At the conclusion of data collection, animals were euthanized (Euthasol, 120 mg/kg, IV) and underwent transcardial perfusion with phosphate-buffered saline, 4% paraformaldehyde fixative, and fixative with 10% sucrose. The brain and spinal cord were removed and sectioned on a freezing microtome. The spinal cord tissue was processed in series for myelin staining (Gallyas 1979) and CTB tracer labels. Immunohistochemistry for CTB tracer was performed for both the spinal cord and brainstem following published procedures (Qi and Kaas 2006). We used NIH ImageJ to measure CTB-labeled areas in the left and right cuneate nuclei of the brainstem across digitally scanned images of brain sections. The ratio of the sum of the area from each side was used to estimate the percentage of the dorsal column afferent disruption following the injury. Details of the histological validation procedures have been published previously (Qi et al. 2011).

To evaluate the impact of DCL, lesion extent determined by histology was correlated with both tactile stimulus-evoked LFP power and rsFC using Pearson correlation and linear regression analyses. Eight monkeys (SM1–SM6 and SM8–SM9) were included in the histology versus LFP power analysis, whereas six monkeys (SM1–SM6) were included in the histology versus rsFC analysis. For the histology-rsFC correlation, only C6 data from post-injury weeks 1 to 3 were included, as behavioral deficits were most prominent during this period.

3 | Results

A total of 272 LFP recording sessions, including 132 trials of vibrotactile stimulation and 140 trials of resting state, were obtained from control monkeys ($n = 4$) and injured monkeys at 3-months ($n = 2$) and 6-months ($n = 7$) post-injury. We first examined the effects of DCL on tactile stimulus-evoked LFP power and functional connectivity measured by LFP coherence among six gray matter regions of interest (ROIs) and then compared them directly with rsFC measures by fMRI. In the end, we related rsFC and LFP coherence measures to the degree of dorsal column afferent disruption quantified by histology across animals. We have previously reported global-scale rsfMRI observations within the primate cervical segments in healthy and DCL conditions (Chen et al. 2015; Sengupta et al. 2021; Wu et al. 2019). Thus, we focus on the comparisons to validate rsfMRI rsFC findings in relation to neuronal LFP measures and anatomical measures.

3.1 | Effects of DCL on Tactile Stimulus-Evoked LFP Power

To understand the effects of unilateral DCL on the responsiveness of spinal gray matter to afferent inputs, we recorded LFP power from the dorsal horns on both the lesion and non-lesion sides during 8 Hz vibrotactile indentation of the fingers and compared them between normal animals and monkeys with DCL injury. The LFP powers in broadband (Figure 1) and five specific frequency bands (Figure S2) were plotted as a function of control, 3 months post-injury, and 6 months post-injury groups. On the lesion side, stimulus-evoked LFP power changes in the dorsal horn significantly decreased in all frequency bands at the 3- and 6-month post-injury time points, compared to the normal dorsal horn (Figure 1D, $^{**}p < 0.005$, $^{****}p < 0.0001$, One-way ANOVA test).

On the non-lesion side, stimulus-evoked LFP power changes in the dorsal horn were similar to normal controls (Figure 1E), with no significant differences in power changes for all frequency bands. For the broadband (Figure 2E) and across five specific frequency bands (Figure S2B), the LFP power changes at 6 months post-injury tended to be lower than those of the normal cord and at 3 months post-injury. However, these power reduction trends were not statistically significant (Figures 1E and S2B). Unilateral DCL thus significantly disrupted tactile stimulation-evoked LFP power changes in dorsal horns on the lesion side, but not on the non-lesion side overall.

Direct comparisons of LFP power changes on the lesion side versus non-lesion side revealed significant power reductions on the lesion side at both 3 months and 6 months post-injury times, which were pronounced in broadband (Figure 1F,G) and across five frequency bands (Figure S2C,D). Thus, the non-lesion side was significantly more responsive to tactile stimulation than the lesion side across all conditions tested ($^{*}p < 0.05$, $^{****}p < 0.0001$, unpaired t-test).

3.2 | Effects of DCL on Resting-State LFP Coherence Between Dorsal-To-Dorsal (D-D) and Ventral-To-Ventral (V-V) Horns

We computed resting-state LFP coherences between gray matter dorsal horns (D-D) among normal, 3 months post-injury, and 6 months post-injury cases. There were no significant differences

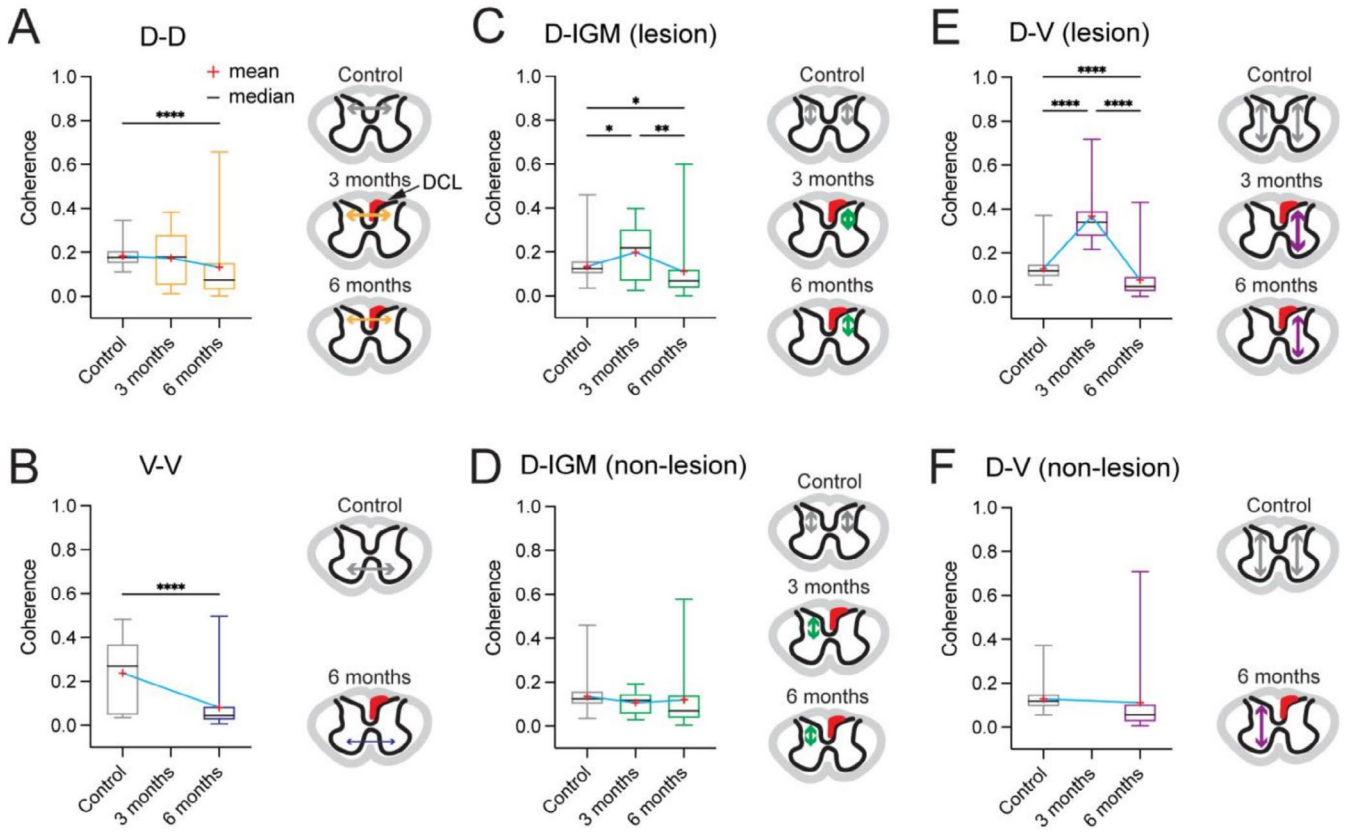

FIGURE 2 | Time courses of lesion effects on the LFP coherence between ROI pairs at rest within the spinal segment below the lesion. (A–F) Box plots show group-averaged broadband LFP coherences across different ROI pairs: Dorsal-to-dorsal (D-D) (A), ventral-to-ventral (V-V) (B), dorsal-to-intermediate zone on the lesion side (D-IGM, lesion) (C), dorsal-to-intermediate zone on the non-lesion side (D-IGM, non-lesion) (D), dorsal-to-ventral on the lesion side (D-V, lesion) (E), and dorsal to ventral on the non-lesion side (D-V, non-lesion) (F). Groups: Control ($n = 4$ monkeys), 3 months post-lesion ($n = 2$), and 6 months post-lesion ($n = 7$). Statistical analyses were conducted using Brown-Forsythe ANOVA with a Dunnett test (A, C, D, E) or unpaired *t*-test (B, F). Significance levels: $^{*}p < 0.05$, $^{***}p < 0.0005$, $^{****}p < 0.0001$.

between normal and 3 months post-injury cases. No significant LFP power changes were detected in the gamma frequency band ($p > 0.2$) between groups (Figure S3A). We found significant decreases in LFP coherence between dorsal horns on the lesion versus non-lesion sides in broadband between normal and DCL cases at 6 months post-injury ($p < 0.0001$, Figure 2A) and all frequency bands between control and DCL cases at 6 months post-injury and between 3 months versus 6 months post-injury. Coherence differences were significant in delta, theta, alpha, and beta bands ($^{**}p < 0.005$, $^{***}p < 0.0005$, $^{****}p < 0.0001$, Figure S3A).

For the ventral horns on the lesion versus non-lesion side (V-V), significant decreases in LFP coherences were observed for broadband ($p < 0.05$, Figure 2B) and all LFP frequency bands (except theta, $p = 0.071$) between normal and 6 months post-injury cases ($^{***}p < 0.0005$, $^{****}p < 0.0001$, Figure S3B). Note that electrodes did not reach the ventral horns in the 3 months post-lesion cases, and this post-injury time is missing from the quantification. Nevertheless, this finding indicates that unilateral DCL reduced coherence between ventral horns (V-V) even when the injury was a lesion of the dorsal column of the spinal cord. Six months post-injury, LFP coherence between D-D and V-V horns on lesion versus non-lesion sides tended to exhibit resting state coherence reductions.

3.3 | LFP Coherence Between Dorsal Horn and Intermediate Gray Matter Zone (D-IGM) on Lesion and Non-Lesion Sides Decreased

Across frequency bands from 1 to 30 Hz (except broadband, Figure 2C, and gamma band, Figure S4C), LFP coherence between the dorsal horn and intermediate gray matter zones (D-IGM) at 6 months post-injury was significantly lower than in normal cases on both the lesion and non-lesion (Figures 2C and S4C) sides. The LFP coherence changes at 3 months post-injury differed. On the lesion side, LFP connectivity at 3 months post-injury was comparable to that of normal cases but was significantly stronger than at 6 months post-injury (Figure 2C). This finding indicates that drastic reductions in LFP coherence between the dorsal and intermediate zones were most pronounced during the 3 to 6 months post-injury period. Conversely, on the non-lesion side, coherence between the dorsal and intermediate zones in the broadband was not significantly changed (Figure 2D), while coherences in the delta, theta, alpha, and beta frequency bands were significantly reduced at both 3 months and 6 months after DCL compared to normal control cases (Figure S4B). Coherence remained lower between 3- and 6-months post-injury for the delta, theta, and beta frequency bands. Only the alpha band showed a continued decrease in LFP coherence from 3 to 6 months post-injury (Figure S4B). This

suggests that significant LFP connectivity changes occurred within the first 3 months post-injury, while all frequency bands (except alpha) showed stable LFP coherence after 3 months post-injury. The lesion and non-lesion sides exhibited different temporal patterns.

Broadband and gamma band frequencies behaved differently from the rest of the LFP frequencies. On the lesion side, coherence was significantly higher in cases at 3 months post-injury than in normal or 6 months post-injury cases (Figure 2C), suggesting coherence in these frequency bands returned to the normal level at 6 months post-injury. On the non-lesion side, broadband (Figure 2D) and gamma band (Figure S4B) show no significant differences between normal controls, 3 months, and 6 months post-injury cases, indicating that unilateral DCL may have limited effects on gamma frequency coherence.

3.4 | Effects of DCL on LFP Coherence Between Dorsal to Ventral Horns (D-V) on Both Lesion and Non-Lesion Sides

Between dorsal and ventral (D-V) horns on the lesioned side of the spinal cord, LFP coherence decreased in broadband (Figure 2E) and across all frequency bands (Figure S4C) at 6 months post-injury, compared to 3 months post-injury and control cases. However, LFP coherences in broadband, alpha, beta, and gamma bands at 3 months post-DCL were significantly higher than those in normal cases (Figures 2E and S4C). LFP coherence across the three groups showed a pattern of connectivity increase at 3 months and decrease at 6 months post-injury.

On the non-lesion side, broadband coherences did not significantly change (Figure 2F), but coherences were significantly lower at 6 months post-injury across most frequency bands, except for gamma frequencies, compared to controls (Figure S4D).

We summarize the overall LFP findings in Figure 3. Most significant changes occurred at 6 months post-injury. Significant LFP power decreases were observed on the lesion side.

3.5 | Effects of DCL on fMRI rsFC Between Spinal Horn Pairs

We examined and compared the rsFC strengths, measured by correlation coefficients (*r* values), between six ROI pairs at pre-lesion, 1–9 weeks post-injury (approximately 3 months), and 16–32 weeks post-injury (approximately 6 months). Figure 4A shows the location of the spinal segments (slices 4 and 5, equal to C6 and C7 spinal segments) included in the rsFC analysis (top image) and the ROIs included in the analysis (bottom two images). These spinal segments receive afferent inputs, primarily from digits 1 and 2 (D1 and D2).

We quantified rsFC on C6 (Slice 4, Figure 4B–G) and C7 (Slice 5, Figure 4H–M) separately to examine the effects of DCL along the spinal cord length below the injury level. For spinal cord

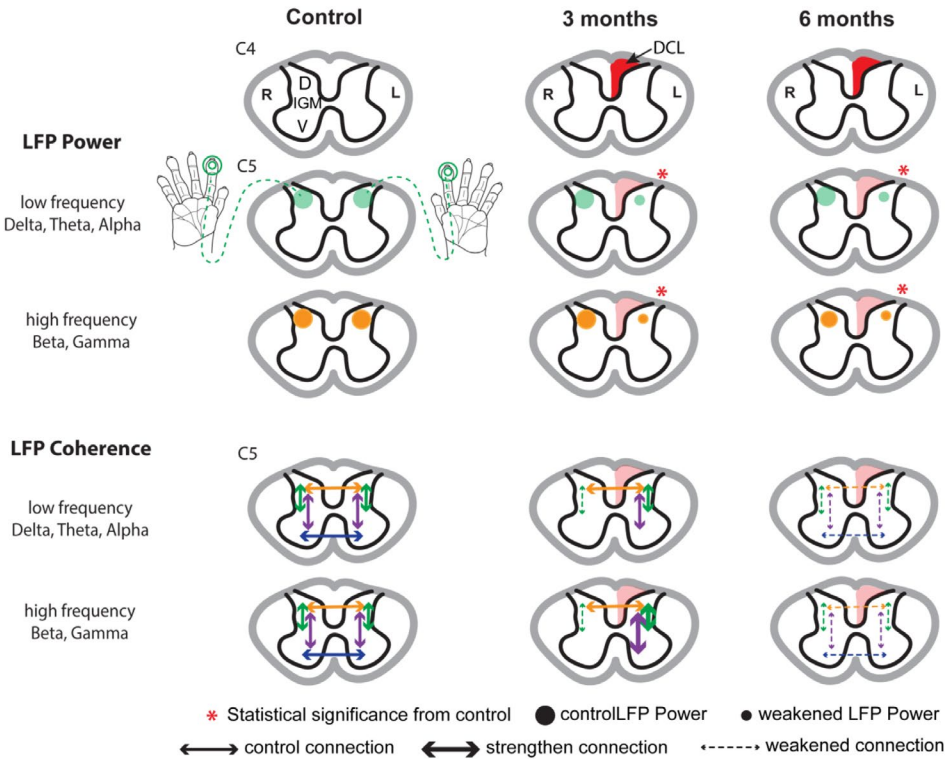

FIGURE 3 | Schematic summary of LFP power and coherence observations. A dorsal column lesion was placed at the C4 level, and LFP signals were recorded from the C5 segment immediately below the lesion. Changes in low-frequency (delta, theta, and alpha) and high-frequency (beta and gamma) LFP signals are illustrated separately. Smaller dots indicate reduced LFP power in response to tactile stimulation of fingertips. Thicker lines represent increased resting state coherence. Red asterisks (*) indicate statistically significant changes from the non-lesion normal animals.

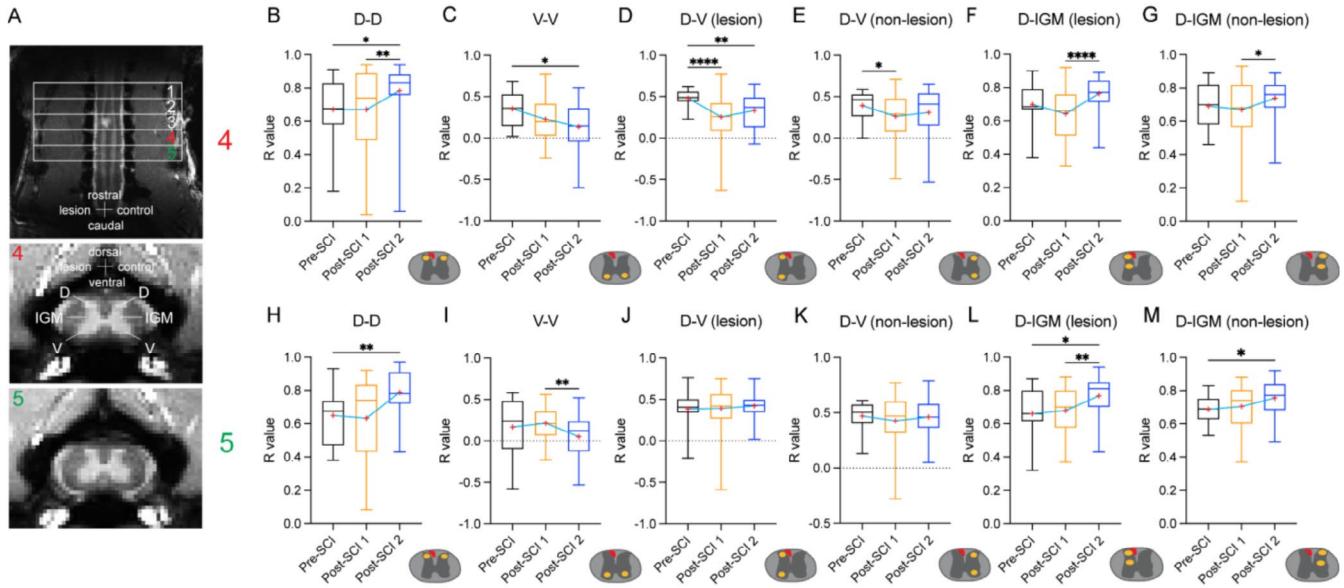

FIGURE 4 | Changes in inter-ROI fMRI resting state functional connectivity (rsFC) over time before and after DCL in two spinal cord segments below the lesion level. (A) The coronal MTC image (top) shows the placements of five transverse imaging slices (middle and bottom). A hyperintensity (indicating lesion) was detected in the middle slice (slice 3) in one representative animal 4 weeks post-injury. (B-M) Plots of correlation coefficients (r values) of resting state fMRI signals between each of the six ROI pairs for slices 4 (C6, B-G) and 5 (C7, H-M) below the lesion level are shown at times from Pre-SCI, Post-SCI 1 (1–9 weeks post-injury), and Post-SCI 2 (16–32 weeks post-injury). Graphics of the spinal cord below each plot indicate the selected ROI pairs (orange dots) relative to the side of the lesion (red). Statistical analyses were performed using the Brown-Forsythe ANOVA, followed by a Dunnett test. Significance levels: *$p < 0.05$, **$p < 0.005$, ****$p < 0.0001$.

ROI pairs on slice 4 at the C6 level, functional connectivity was significantly strengthened for D-D (Figure 4B) but significantly weakened for V-V and D-V on the lesion side at 16–32 weeks post-injury (Figure 4C,D). At the 1–9 weeks post-injury time point, significant rsFC weakening was observed only in D-V on the lesion side.

For ROI pairs on slice 5 at the C7 level, the effects of DCL were much weaker in general. Conversely, the rsFC connectivity strength was significantly stronger for ROI pairs of D-D and D-IGM on both lesion and non-lesion sides. Ventral-to-ventral (V-V) horn connectivity tended to be weaker; however, the changes were not significant ($p = 0.65$). The overall pattern for rsFC changes across spinal segments (from C6 to C7) differed drastically, indicating that rsFC changes are distance-dependent. The only common change between C6 and C7 was the enhancement at 6 months post-injury (compare Figure 4B,H).

3.6 | Relationship Between Changes in LFP Coherence and fMRI rsFC After Injury

We plotted broadband LFP coherence against rsFC r values for all six ROI pairs across all pre- and post-injury time points and examined the correlative relationship between these two measures of functional connectivity (Figure 5). Figure 5A–F display the trends of LFP and rsFC for each of the six ROI pairs. The overall trend of connectivity changes between V-D horns on the lesion side differed from the rest of the ROI pairs. The correlation between correlation coefficients of rsFC and LFP coherences was $r = 0.52$ when two outliers (V-V and D-V on the lesion side) were excluded in the analysis (Figure 5G,H). Standard statistical diagnostics were performed using GraphPad Prism (iterative Grubbs' test, alpha = 0.2) to identify outliers. The results indicate that changes in LFP and rsfMRI connectivity showed a trend toward correlation, but the relationship did not reach statistical significance ($r = 0.52$, $p = 0.057$).

The two missing data points in Figure 5G,H are attributed to the "dead space" at the tip of the linear electrode array used in this study. In some sessions, the electrode could not sample LFPs from the ventral horn because of placement constraints or anatomical variability. This issue is also evident in Figure 5B,D, where no LFP coherence was obtained at the Post-SCI 1 time point.

3.7 | The Extent of Lesions Assessed by Histology and Their Correlations With Connectivity Reduction

Histology data were acquired months after a unilateral DCL was placed at the level of C4 to C5, a location that is above the cervical enlargement. The DCL was intended to disrupt all ascending afferents in the dorsal column tract on one side of the spinal cord. Figure 6A shows examples of CTB staining at the cuneate nucleus from three monkeys, which showed 81% (SM2), 99% (SM5), and 100% (SM7) deprivation of afferents from the fingers. Figure 6B displayed the myelin stain showing the loss of myelin at the dorsal column tract location rostral to the spinal cord level where the lesion was placed. Overall, histological evaluation of the CTB-tracer label confirmed that 7 out of 10 monkeys with DCL had lesions that disrupted 99% or more of the axons in the dorsal column pathway that terminates in the brainstem cuneate nucleus. Two of the monkeys had about 80% disruption

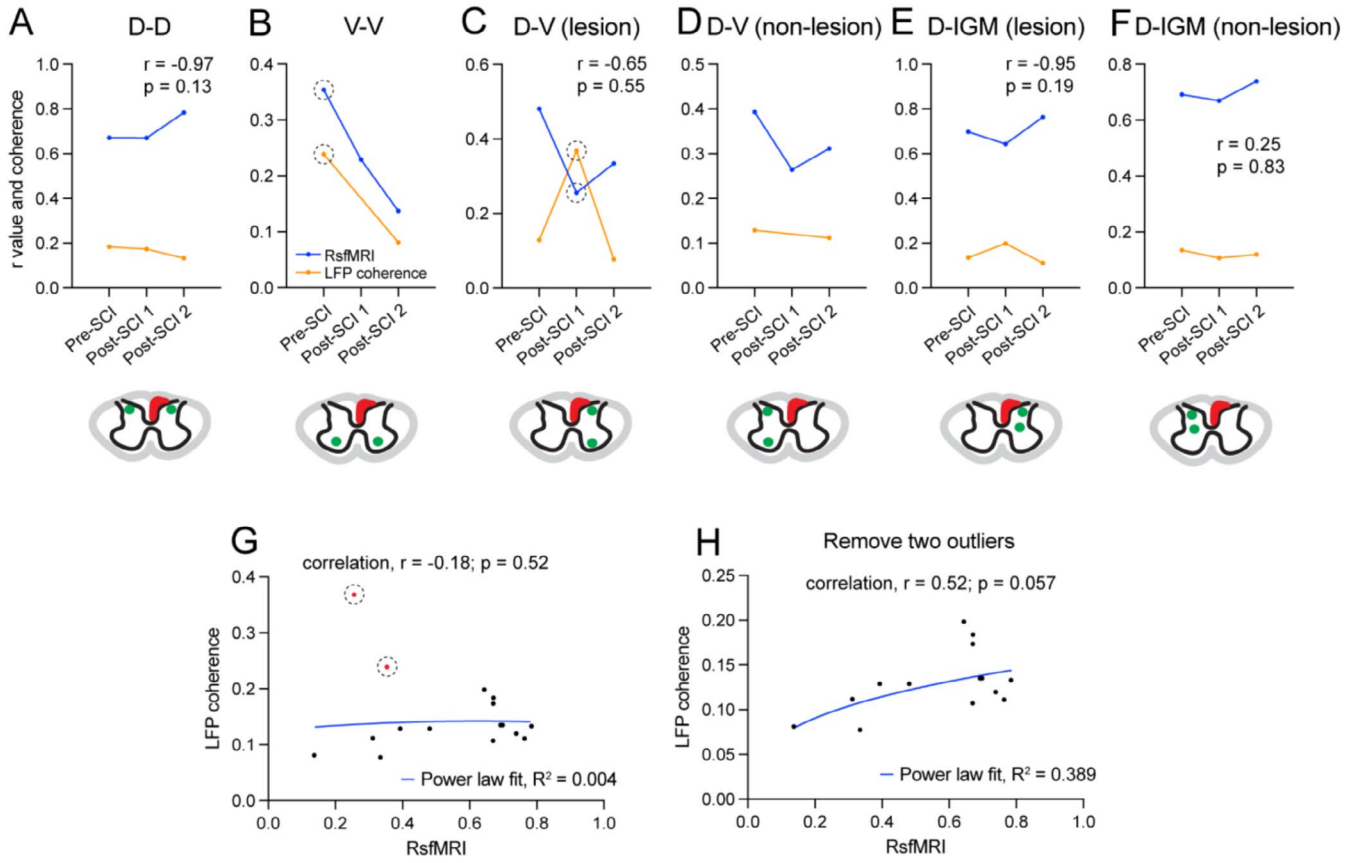

FIGURE 5 | Relationship between broadband LFP coherence and rsFC across six ROI pairs in the C5 segment. (A–F) Line plots show the rsFC *r* values (blue) and LFP coherence (orange) across different time points for each of the six ROI pairs. (G, H) Scatter plots display LFP coherence versus rsFC values across all ROI pairs: (G) includes pre- and post-injury time points (Post-SCI 1 and Post-SCI 2 with data from 3 and 6 months, respectively), while (H) shows the same data with two outliers removed. Outliers selected using GraphPad Prism iterative Grubbs' test (alpha = 0.2; V-V and D-V on the lesion side, marked as red dots in G). Blue lines represent power law fits. Pearson correlation coefficients (r) and *p*-values are reported. The total number of data points is 16 in (G) and 14 in (H).

of the dorsal column pathway (81% in SM2, 78% in SM7). In one of the monkeys (SM8), CTB tracer was not injected in the digits; therefore, the percentage of the primary somatosensory pathway that was disrupted could not be quantified based on CTB-label differences between the left and right sides. Lesions were primarily restricted to the somatosensory representations of the dorsal white matter but also disrupted portions of the dorsal horn gray matter extending into the intermediate gray and ventral horn. There was no apparent relationship between the degree of DCL and changes in LFP power or correlation strength of rsFC between the D-D ROI pairs (Figure 6C,D).

4 | Discussion

4.1 | Bilateral Effects of Unilateral DCL on Dorsal Horn LFP Responses to Tactile Stimulation

A unilateral DCL at the rostral end of the cervical enlargement selectively disrupts ascending afferents that carry discriminant vibrotactile information from the hand to the cuneate nucleus and then to the brain (Darian-Smith 2007; Qi et al. 2013, 2014; Wang et al. 2015; Wu et al. 2017). In this study, we purposely placed the DCL at the C4 level, rostral to the cervical enlargement (C5–C7), to disrupt ascending inputs originating in the dorsal horns that receive afferents from the hand and digits. This design ensures selective disruption of the somatic ascending pathway without affecting other pathways that carry information from the hand to the brain from the spinal cord. We targeted segments immediately caudal to the DCL because our prior cervical-spinal-cord fMRI showed that a DCL at the C4 level primarily disrupted the rsFC in segments below the lesion.

On the lesion side, dorsal horn responsiveness (LFP power) to hand tactile stimulation was significantly reduced across broadband and individual frequency bands at 6 months post-DCL. At 3 months, reductions were detectable but weaker, reaching significance only for broadband and high-frequency beta/gamma bands (Figure 1). Thus, broadband and high-frequency beta and gamma LFP band power appeared to be sensitive indicators of the disrupted ascending DCL pathway.

Notably, LFP power in broadband and beta bands on the non-lesion side was also reduced at 6 months, indicating a cross-midline effect in segments below the DCL. Histology confirmed the lesion was spatially constrained to the intended side, suggesting that these cross-midline effects are mediated by either inter-segmental connections and/or top-down influences from top-down sources (such as brainstem). The marked beta/gamma reductions align well with the view that higher frequencies

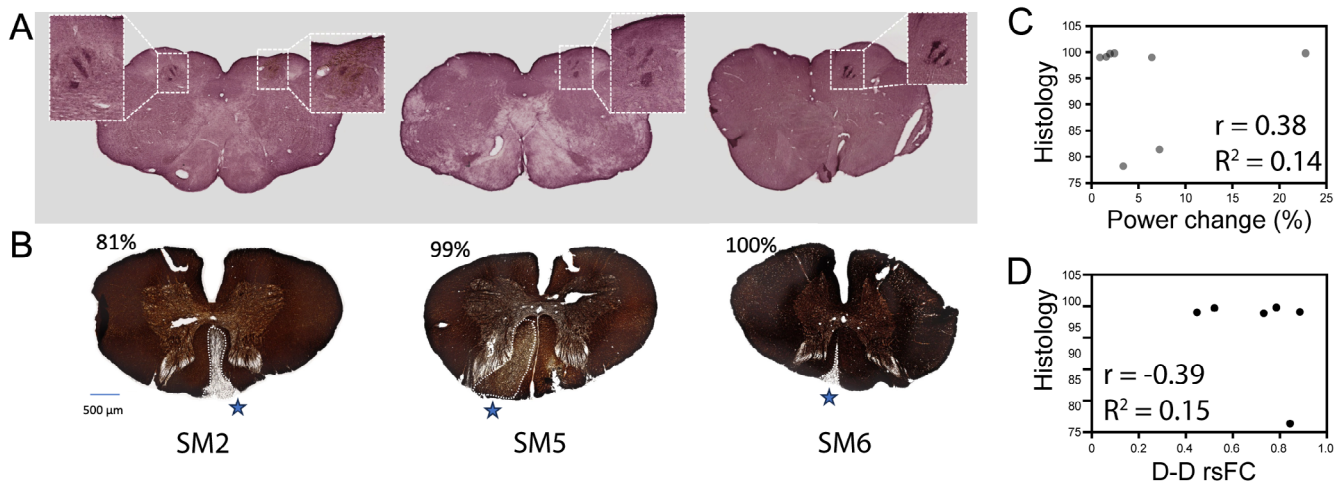

FIGURE 6 | Post-mortem histology validates and quantifies the extent of the dorsal column lesion. Three representative cases are shown. (A) CTB stains show tracer uptake on both sides of the dorsal column nucleus in the brainstem after CTB injection into left and right digits 1, 3, and 5. (B) Myelin stains of the spinal cord sections rostral to the injury reveal demyelination of dorsal column tracts, indicated by light staining (stars). Percentage indicates the disrupted afferents as quantified by comparing CTB staining in the left and right brainstem. (C,D) Plots of LFP power changes and D-D rsFC correlation values as a function of the percentage of dorsal column fiber disruption across all cases.

carry sensory processing signals (Jia and Kohn 2011; Welle and Contreras 2016; Yue et al. 2025).

The gamma band is of particular interest because of its established link to sensory processing in the brain (Fries 2015; Zhang et al. 2012). To our knowledge, there is limited literature specifically examining spinal gamma oscillations, particularly in non-human primates. In rodent models of spinal cord injury (SC), sustained increases in gamma-band LFP power in the motor cortex were observed during skilled reaching training compared to injured controls and in the cortex of patients with disorders of consciousness during spinal cord stimulation (Bai et al. 2017a, 2017b; Salimi et al. 2021). This provides evidence of gamma-band modulation within the spinal-brain networks associated with behavior and SC injury.

4.2 | Temporal Dynamics of Spinal Cord Functional Connectivity Measured by LFP

Building on prior work showing early (≤4 weeks) rsFC changes after injury (Sengupta et al. 2021), we observed dynamic changes in LFP coherence over 3–6 months. On the lesion side, connectivity between dorsal (D-D), ventral (V-V), and dorsal to intermediate zone (D-IGM), and dorsal to ventral (D-V) pairs was broadly weaker by 6 months and entered a stable phase, whereas at 3 months, the recovery pattern was mixed, in which D-V pairs showed increased coherence across most of the LFP frequency bands, including gamma and broadband (Figure 2).

On the non-lesion side, connectivity also weakened across ROI pairs, indicating general bilateral disruptive effects of unilateral DCL on the spinal functional connectivity. Figure 3 illustrates the summary of the general findings. The agreement between reduced LFP power and functional connectivity disruption supports the theory for spinal cord—established in the brain—that neurons and networks engaged in the same function often show strong resting connectivity (Shi et al. 2017; Wang et al. 2013; Wu et al. 2019), and disruption diminishes it (Chen et al. 2015; Sengupta et al. 2021).

One significant implication of these findings is related to the temporal dynamics of LFP power and connectivity measures over an extended period (6 months) after injury, which may help explain the long-lasting behavioral deficits detected by AI-assisted analyses but not by performance-based global behavioral measures (Duque et al. 2023, 2025). Understanding the mechanisms of such slow-paced dynamic changes associated with long-term behavioral deficits and incomplete recovery is important for developing treatments for SCI, where recovery can take months to years.

Reduced tactile-evoked and spontaneous LFP power in spinal cord caudal to (or below) the lesion likely can be explained by four mechanisms: First, although the DCL does not directly affect the primary afferent input entering the spinal cord below the lesion site, it disrupts the major ascending pathway responsible for transmitting tactile information to supraspinal structures. Disruption of the transmission at the secondary relay neurons could affect the processing of incoming tactile inputs from the hand at the dorsal horn, for example, through modulation of the local excitability of neurons and circuits (Deumens et al. 2013; Harding et al. 2020). The second mechanism involves local white-matter and inter-segmental effects. Surgical sectioning of the dorsal column fibers likely also alters neighboring intraspinal white matter tracts and affects functional modulation from C3 centers to the below-lesion C5–C7 hand segments (Alstermark et al. 1999; Burke et al. 1992, 1994; Maier et al. 1998). The dorsal column transaction disrupted this descending control and inter-segmental connections. Third, altered supraspinal drive and reorganization could affect the spinal cord processing. Using the same DCL model, our previous brain fMRI studies have revealed brain-wide reorganization of the somatosensory system and beyond (Chen et al. 2012; Qi et al. 2011). Moreover, there have been reports that the somatosensory cortex in rodents and NHPs exerts direct control over dorsal horn neurons via direct connections (Frezel et al. 2020;

Galea and Darian-Smith 1994; Ralston and Ralston 3rd 1985; Ueno et al. 2018). A fourth possible mechanism is changes in spinal cord state or baseline tonic firing activity. The disconnection between the brain and the cervical spinal cord could induce widespread functional reorganization of spinal cord circuits, including altered excitability or tonic firing of neurons. As such, the reduced evoked and spontaneous LFP power we observed below the lesion likely reflects both disrupted long-range signaling and local network alterations.

4.3 | Correlative Relationship Between Changes in rsFC and LFP Coherence Following Spinal Cord Injury

MRI permits coverage across multiple spinal cord segments above and below the lesion. Here, we focused LFP signal sampling on the segment immediately below the injury (C6) and related longitudinal changes in LFP coherence to rsFC (Figure 5). This focus is driven by prior evidence that rsFC alterations occurred primarily in segments below the lesion (Chen et al. 2015). We found a trend of correlation ($r = 0.52$, $p = 0.057$) between rsFC and LFP changes across ROI pairs and time points, consistent with findings in the healthy spinal cord of the same animal model (Wu et al. 2019). This supports the utility of rsFC as a noninvasive index of inter-regional functional integrity of the spinal cord in both healthy and injured states (Chen et al. 2015; Wu et al. 2019).

A close examination of the C6 segment, which receives ascending inputs from digits 2 and 3, revealed four patterns of LFP-rsFC temporal relationships after injury: (1) correlated strengthening, (2) correlated weakening, (3) enhanced rsFC with reduced LFP, and (4) reduced rsFC with enhanced LFP. For example, non-lesion-side V-V and D-V connectivity weakened; non-lesion-side D-IGM strengthened; D-D showed increased rsFC but decreased LFP coherence; and lesion-side D-V showed increased broadband and high-frequency (alpha, beta, and gamma) LFP coherence with reduced rsFC. These divergent patterns highlight the complexity of plasticity following selective disruption of somatosensory afferents and are in line with frequency-specific roles reported in various pathological conditions (Brown and Williams 2005; Morelli 2023; Morelli and Summers 2023; Strelow et al. 2023; Thompson et al. 2014). We extend this notion from the brain to the spinal cord with traumatic injury.

Our rsFC results also suggest that the effects of spinal cord injury on functional connectivity wane with distance from the lesion. For example, at C7 (slice 5), which is one segment further caudal from the segment where LFP recordings were obtained (at C6 slice 4), caudal to the lesion level (at C5), rsFC showed distinct post-injury trends, with only a consistent increase in D-D (Figure 4H). No significant changes were observed in ROI pairs that had shown reduced connectivity at C6. Additionally, dorsal horn to intermediate zone (D-IGM) connections at C7 exhibited enhanced rsFC, mirroring the trend seen in the C6 segment. Overall, a trend of rsFC-LFP correlation at the C6 level was evident on a slower, months-long time scale. Future work with simultaneous recording will be needed for direct validation.

4.4 | Limitations of the Study

Because data acquisition was interleaved, LFPs were collected at only two time points (~3- and 6-months post-injury), and fMRI and LFP measurements were separated by several weeks. This temporal mismatch likely reduced the statistical power of the temporal correlation analysis. We demonstrated here that long-term cross-model studies are feasible. A future study with a larger sample size will enable more definitive conclusions.

5 | Conclusion

Selective unilateral DCL reduces the stimulus-evoked LFP power in the dorsal horn and weakens inter-regional gray-matter connectivity beyond the lesion side. LFP coherence and rsFC connectivity collected before injury and at times around 3 months and 6 months post-injury help to support—but not yet statistically confirm—the interpretation that rsfMRI rsFC can be used as a surrogate of neural functional connectivity and as a biomarker of circuit-level integrity in the cervical spinal cord of nonhuman primates. The results indicate that changes in LFP and rsfMRI connectivity show a trend toward correlation, but the relationship did not reach statistical significance. The markedly different inter-regional rsFC patterns observed in segments more caudal to the lesion underscore the complexity of network-level recovery. Clarifying the mechanisms behind these changes will be important for guiding the development of therapeutic interventions for SCI.

Acknowledgments

This study was funded by NIH NINDS grant 2R01NS078680. We thank Ms. Chaohui Tang for her assistance with animal care and data acquisition, and we acknowledge the valuable contributions of Chaohui Tang, Dr. Huixin Qi, and Laura Trice to the histology work.

Ethics Statement

All procedures conducted in this research were approved by the Institutional Animal Care and Use Committee at Vanderbilt University and followed NIH guidelines.

Conflicts of Interest

The authors declare no conflicts of interest.

Data Availability Statement

The data that support the findings of this study are available on request from the corresponding author. The data are not publicly available due to privacy or ethical restrictions.

References

Alstermark, B., T. Isa, Y. Ohki, and Y. Saito. 1999. "Disynaptic Pyramidal Excitation in Forelimb Motoneurons Mediated via C(3)-C(4) Propriospinal Neurons in the *Macaca fuscata*." *Journal of Neurophysiology* 82, no. 6: 3580–3585. https://doi.org/10.1152/jn.1999.82.6.3580.

Bai, Y., X. Xia, Z. Liang, et al. 2017a. "Corrigendum: Frontal Connectivity in EEG Gamma (30-45 Hz) Respond to Spinal Cord Stimulation in Minimally Conscious State Patients." *Frontiers in Cellular Neuroscience* 11: 251. https://doi.org/10.3389/fncel.2017.00251.

Bai, Y., X. Xia, Z. Liang, et al. 2017b. "Frontal Connectivity in EEG Gamma (30-45 Hz) Respond to Spinal Cord Stimulation in Minimally Conscious State Patients." *Frontiers in Cellular Neuroscience* 11: 177. https://doi.org/10.3389/fncel.2017.00177.

Barry, R. L., B. N. Conrad, S. A. Smith, and J. C. Gore. 2018. "A Practical Protocol for Measurements of Spinal Cord Functional Connectivity." *Scientific Reports* 8, no. 1: 16512. https://doi.org/10.1038/s41598-018-34841-6.

Barry, R. L., B. P. Rogers, B. N. Conrad, S. A. Smith, and J. C. Gore. 2016. "Reproducibility of Resting State Spinal Cord Networks in Healthy Volunteers at 7 Tesla." *Neuroimage* 133: 31–40. https://doi.org/10.1016/j.neuroimage.2016.02.058.

Brown, P., and D. Williams. 2005. "Basal Ganglia Local Field Potential Activity: Character and Functional Significance in the Human." *Clinical Neurophysiology* 116, no. 11: 2510–2519. https://doi.org/10.1016/j.clinph.2005.05.009.

Burke, D., J. M. Gracies, D. Mazevet, S. Meunier, and E. Pierrot-Deseilligny. 1992. "Convergence of Descending and Various Peripheral Inputs Onto Common Propriospinal-Like Neurones in Man." *Journal of Physiology* 449: 655–671. https://doi.org/10.1113/jphysiol.1992.sp019107.

Burke, D., J. M. Gracies, D. Mazevet, S. Meunier, and E. Pierrot-Deseilligny. 1994. "Non-Monosynaptic Transmission of the Cortical Command for Voluntary Movement in Man." *Journal of Physiology* 480, no. Pt 1: 191–202. https://doi.org/10.1113/jphysiol.1994.sp020352.

Calhoun, V. D., T. Adali, G. D. Pearlson, and J. J. Pekar. 2001. "A Method for Making Group Inferences From Functional MRI Data Using Independent Component Analysis." *Human Brain Mapping* 14, no. 3: 140–151. https://doi.org/10.1002/hbm.1048.

Chen, L. M., A. Mishra, P. F. Yang, F. Wang, and J. C. Gore. 2015. "Injury Alters Intrinsic Functional Connectivity Within the Primate Spinal Cord." *Proceedings of the National Academy of Sciences of the United States of America* 112, no. 19: 5991–5996. https://doi.org/10.1073/pnas.1424106112.

Chen, L. M., H. X. Qi, and J. H. Kaas. 2012. "Dynamic Reorganization of Digit Representations in Somatosensory Cortex of Nonhuman Primates After Spinal Cord Injury." *Journal of Neuroscience* 32, no. 42: 14649–14663. https://doi.org/10.1523/JNEUROSCI.1841-12.2012.

Combes, A., L. Narisetti, A. Sengupta, et al. 2023. "Detection of Resting-State Functional Connectivity in the Lumbar Spinal Cord With 3T MRI." *Scientific Reports* 13, no. 1: 18189. https://doi.org/10.1038/s41598-023-45302-0.

Combes, A. J. E., K. P. O'Grady, B. P. Rogers, et al. 2022. "Functional Connectivity in the Dorsal Network of the Cervical Spinal Cord Is Correlated With Diffusion Tensor Imaging Indices in Relapsing-Remitting Multiple Sclerosis." *NeuroImage: Clinical* 35: 103127. https://doi.org/10.1016/j.nicl.2022.103127.

Darian-Smith, C. 2007. "Monkey Models of Recovery of Voluntary Hand Movement After Spinal Cord and Dorsal Root Injury." *ILAR Journal* 48, no. 4: 396–410. https://doi.org/10.1093/ilar.48.4.396.

Deumens, R., G. L. Mazzone, and G. Taccola. 2013. "Early Spread of Hyperexcitability to Caudal Dorsal Horn Networks After a Chemically-Induced Lesion of the Rat Spinal Cord in Vitro." *Neuroscience* 229: 155–163. https://doi.org/10.1016/j.neuroscience.2012.10.036.

Duque, D. H., J. M. Racca, I. V. Manzanera Esteve, P. F. Yang, J. C. Gore, and L. M. Chen. 2023. "Machine-Learning-Based Video Analysis of Grasping Behavior During Recovery From Cervical Spinal Cord Injury." *Behavioural Brain Research* 443: 114150. https://doi.org/10.1016/j.bbr.2022.114150.

Duque, D. H., P. F. Yang, J. C. Gore, and L. M. Chen. 2025. "AI-Assisted 3D Analysis of Grasping and Reaching Behavior of Squirrel Monkeys During Recovery From Cervical Spinal Cord Injury." *Behavioural Brain Research* 476: 115265. https://doi.org/10.1016/j.bbr.2024.115265.

Frezel, N., E. Platonova, F. F. Voigt, et al. 2020. "In-Depth Characterization of Layer 5 Output Neurons of the Primary Somatosensory Cortex Innervating the Mouse Dorsal Spinal Cord." *Cerebral Cortex Communications* 1, no. 1: tgaa052. https://doi.org/10.1093/texcom/tgaa052.

Fries, P. 2015. "Rhythms for Cognition: Communication Through Coherence." *Neuron* 88, no. 1: 220–235. https://doi.org/10.1016/j.neuron.2015.09.034.

Galea, M. P., and I. Darian-Smith. 1994. "Multiple Corticospinal Neuron Populations in the Macaque Monkey Are Specified by Their Unique Cortical Origins, Spinal Terminations, and Connections." *Cerebral Cortex* 4, no. 2: 166–194. https://doi.org/10.1093/cercor/4.2.166.

Gallyas, F. 1979. "Silver Staining of Myelin by Means of Physical Development." *Neurological Research* 1, no. 2: 203–209. https://doi.org/10.1080/01616412.1979.11739553.

Glover, G. H., T. Q. Li, and D. Ress. 2000. "Image-Based Method for Retrospective Correction of Physiological Motion Effects in fMRI: RETROICOR." *Magnetic Resonance in Medicine* 44, no. 1: 162–167. https://doi.org/10.1002/1522-2594(200007)44:1<162::aid-mrm23>3.0.co;2-e.

Harding, E. K., S. W. Fung, and R. P. Bonin. 2020. "Insights Into Spinal Dorsal Horn Circuit Function and Dysfunction Using Optical Approaches." *Frontiers in Neural Circuits* 14: 31. https://doi.org/10.3389/fncir.2020.00031.

Jenkinson, M., and S. Smith. 2001. "A Global Optimization Method for Robust Affine Registration of Brain Images." *Medical Image Analysis* 5, no. 2: 143–156. https://doi.org/10.1016/s1361-8415(01)00036-6.

Jia, X., and A. Kohn. 2011. "Gamma Rhythms in the Brain." *PLoS Biology* 9, no. 4: e1001045. https://doi.org/10.1371/journal.pbio.1001045.

Kinany, N., E. Pirondini, S. Micera, and D. Van De Ville. 2020. "Dynamic Functional Connectivity of Resting-State Spinal Cord fMRI Reveals Fine-Grained Intrinsic Architecture." *Neuron* 108, no. 3: 424–435. https://doi.org/10.1016/j.neuron.2020.07.024.

Kinany, N., E. Pirondini, S. Micera, and D. Van De Ville. 2023. "Spinal Cord fMRI: A New Window Into the Central Nervous System." *Neuroscientist* 29, no. 6: 715–731. https://doi.org/10.1177/10738584221101827.

Kong, Y., F. Eippert, C. F. Beckmann, et al. 2014. "Intrinsically Organized Resting State Networks in the Human Spinal Cord." *Proceedings of the National Academy of Sciences of the United States of America* 111, no. 50: 18067–18072. https://doi.org/10.1073/pnas.1414293111.

Maier, M. A., M. Illert, P. A. Kirkwood, J. Nielsen, and R. N. Lemon. 1998. "Does a C3-C4 Propriospinal System Transmit Corticospinal Excitation in the Primate? An Investigation in the Macaque Monkey." *Journal of Physiology* 511, no. Pt 1: 191–212. https://doi.org/10.1111/j.1469-7793.1998.191bi.x.

Morelli, N. 2023. "Effect and Relationship of Gait on Subcortical Local Field Potentials in Parkinson's Disease: A Systematic Review." *Neuromodulation* 26, no. 2: 271–279. https://doi.org/10.1016/j.neurom.2022.09.001.

Morelli, N., and R. L. S. Summers. 2023. "Association of Subthalamic Beta Frequency Sub-Bands to Symptom Severity in Patients With Parkinson's Disease: A Systematic Review." *Parkinsonism & Related Disorders* 110: 105364. https://doi.org/10.1016/j.parkreldis.2023.105364.

Oostenveld, R., P. Fries, E. Maris, and J. M. Schoffelen. 2011. "FieldTrip: Open Source Software for Advanced Analysis of MEG, EEG, and Invasive Electrophysiological Data." *Computational Intelligence and Neuroscience* 2011: 156869. https://doi.org/10.1155/2011/156869.

Qi, H. X., L. M. Chen, and J. H. Kaas. 2011. "Reorganization of Somatosensory Cortical Areas 3b and 1 After Unilateral Section of Dorsal Columns of the Spinal Cord in Squirrel Monkeys." *Journal of Neuroscience* 31, no. 38: 13662–13675. https://doi.org/10.1523/JNEUROSCI.2366-11.2011.

Qi, H. X., O. A. Gharbawie, K. W. Wynne, and J. H. Kaas. 2013. "Impairment and Recovery of Hand Use After Unilateral Section of the Dorsal Columns of the Spinal Cord in Squirrel Monkeys." *Behavioural Brain Research* 252: 363–376. https://doi.org/10.1016/j.bbr.2013.05.058.

Qi, H. X., and J. H. Kaas. 2006. "Organization of Primary Afferent Projections to the Gracile Nucleus of the Dorsal Column System of Primates." *Journal of Comparative Neurology* 499, no. 2: 183–217. https://doi.org/10.1002/cne.21061.

Qi, H. X., J. H. Kaas, and J. L. Reed. 2014. "The Reactivation of Somatosensory Cortex and Behavioral Recovery After Sensory Loss in Mature Primates." *Frontiers in Systems Neuroscience* 8: 84. https://doi.org/10.3389/fnsys.2014.00084.

Qi, H. X., F. Wang, C. C. Liao, et al. 2016. "Spatiotemporal Trajectories of Reactivation of Somatosensory Cortex by Direct and Secondary Pathways After Dorsal Column Lesions in Squirrel Monkeys." *Neuroimage* 142: 431–453. https://doi.org/10.1016/j.neuroimage.2016.08.015.

Ralston, D. D., and H. J. Ralston 3rd. 1985. "The Terminations of Corticospinal Tract Axons in the Macaque Monkey." *Journal of Comparative Neurology* 242, no. 3: 325–337. https://doi.org/10.1002/cne.902420303.

Salimi, O., H. S. Zangbar, S. H. Shadiabad, et al. 2021. "Forelimb Motor Skills Deficits Following Thoracic Spinal Cord Injury: Underlying Dopaminergic and Neural Oscillatory Changes in Rat Primary Motor Cortex." *ASN Neuro* 13: 17590914211044000. https://doi.org/10.1177/17590914211044000.

Sengupta, A., A. Mishra, F. Wang, et al. 2021. "Functional Networks in Non-Human Primate Spinal Cord and the Effects of Injury." *Neuroimage* 240: 118391. https://doi.org/10.1016/j.neuroimage.2021.118391.

Shi, Z., R. Wu, P. F. Yang, et al. 2017. "High Spatial Correspondence at a Columnar Level Between Activation and Resting State fMRI Signals and Local Field Potentials." *Proceedings of the National Academy of Sciences of the United States of America* 114, no. 20: 5253–5258. https://doi.org/10.1073/pnas.1620520114.

Strelow, J. N., T. A. Dembek, J. C. Baldermann, et al. 2023. "Low Beta-Band Suppression as a Tool for DBS Contact Selection for Akinetic-Rigid Symptoms in Parkinson's Disease." *Parkinsonism & Related Disorders* 112: 105478. https://doi.org/10.1016/j.parkreldis.2023.105478.

Thompson, J. A., D. Lanctin, N. F. Ince, and A. Abosch. 2014. "Clinical Implications of Local Field Potentials for Understanding and Treating Movement Disorders." *Stereotactic and Functional Neurosurgery* 92, no. 4: 251–263. https://doi.org/10.1159/000364913.

Ueno, M., Y. Nakamura, J. Li, et al. 2018. "Corticospinal Circuits From the Sensory and Motor Cortices Differentially Regulate Skilled Movements Through Distinct Spinal Interneurons." *Cell Reports* 23, no. 5: 1286–1300. https://doi.org/10.1016/j.celrep.2018.03.137.

Wang, F., H. X. Qi, Z. Zu, et al. 2015. "Multiparametric MRI Reveals Dynamic Changes in Molecular Signatures of Injured Spinal Cord in Monkeys." *Magnetic Resonance in Medicine* 74, no. 4: 1125–1137. https://doi.org/10.1002/mrm.25488.

Wang, F., Z. Zu, R. Wu, T. L. Wu, J. C. Gore, and L. M. Chen. 2018. "MRI Evaluation of Regional and Longitudinal Changes in Z-Spectra of Injured Spinal Cord of Monkeys." *Magnetic Resonance in Medicine* 79, no. 2: 1070–1082. https://doi.org/10.1002/mrm.26756.

Wang, Z., L. M. Chen, L. Negyessy, et al. 2013. "The Relationship of Anatomical and Functional Connectivity to Resting-State Connectivity in Primate Somatosensory Cortex." *Neuron* 78, no. 6: 1116–1126. https://doi.org/10.1016/j.neuron.2013.04.023.

Welle, C. G., and D. Contreras. 2016. "Sensory-Driven and Spontaneous Gamma Oscillations Engage Distinct Cortical Circuitry." *Journal of Neurophysiology* 115, no. 4: 1821–1835. https://doi.org/10.1152/jn.00137.2015.

Wu, R., P. F. Yang, and L. M. Chen. 2017. "Correlated Disruption of Resting-State fMRI, LFP, and Spike Connectivity Between Area 3b and S2 Following Spinal Cord Injury in Monkeys." *Journal of Neuroscience* 37, no. 46: 11192–11203. https://doi.org/10.1523/JNEUROSCI.2318-17.2017.

Wu, T. L., F. Wang, A. Mishra, et al. 2018. "Resting-State Functional Connectivity in the Rat Cervical Spinal Cord at 9.4 T." *Magnetic Resonance in Medicine* 79, no. 5: 2773–2783. https://doi.org/10.1002/mrm.26905.

Wu, T. L., P. F. Yang, F. Wang, et al. 2019. "Intrinsic Functional Architecture of the Non-Human Primate Spinal Cord Derived From fMRI and Electrophysiology." *Nature Communications* 10, no. 1: 1416. https://doi.org/10.1038/s41467-019-09485-3.

Yue, L., C. Bao, L. Zhang, et al. 2025. "Neuronal Mechanisms of Nociceptive-Evoked Gamma-Band Oscillations in Rodents." *Neuron* 113, no. 5: 769–784. https://doi.org/10.1016/j.neuron.2024.12.011.

Zhang, Z. G., L. Hu, Y. S. Hung, A. Mouraux, and G. D. Iannetti. 2012. "Gamma-Band Oscillations in the Primary Somatosensory Cortex–A Direct and Obligatory Correlate of Subjective Pain Intensity." *Journal of Neuroscience* 32, no. 22: 7429–7438. https://doi.org/10.1523/JNEUROSCI.5877-11.2012.

Supporting Information

Additional supporting information can be found online in the Supporting Information section. **Table S1:** Data acquisition timeline. **Figure S1:** Examples of coregistration between fMRI and MTC structural images. (A, B) functional images before and after alignment to the subject's structural image. (C) functional images of the two subjects aligned to the spinal cord template. **Figure S2:** Temporal dynamics of vibrotactile stimulus-evoked LFP power following dorsal column lesion (DCL) and comparison between lesion and non-lesion sides. (A, B) Box plots showing 8 Hz vibrotactile stimulus-evoked LFP power changes across five specific LFP frequency bands in healthy monkeys ($n = 4$), and at 3 months ($n = 2$) and 6 months ($n = 7$) post-injury on the lesion side (A) and non-lesion side (B). (C, D) Box plots comparing stimulus-evoked LFP power between the lesion and non-lesion sides across five frequency bands at 3 months (C) and 6 months (D) post-injury. Statistical analyses were performed using Brown-Forsythe ANOVA with a Dunnett test or an unpaired *t*-test. Significance levels: $^{*}p < 0.05$, $^{***}p < 0.0005$,$^{****}p < 0.0001$. In each boxplot, the median is shown as a horizontal line and the mean as a red plus symbol. **Figure S3:** Time course of lesion effects on LFP coherence between gray matter horns at resting state within the spinal segment below the lesion. Box plots of group-averaged coherence in five specific frequency bands across two horn pairs: dorsal-to-dorsal (D-D) (A) and ventral-to-ventral (V-V) (B). Control group ($n = 4$ monkeys), 3 months post-injury ($n = 2$), and 6 months post-injury ($n = 7$). Statistical analyses were performed using Brown-Forsythe ANOVA with a Dunnett test or unpaired *t*-test. Significance levels: $^{**}p < 0.005$, $^{***}p < 0.0005$, $^{****}p < 0.0001$. **Figure S4:** Time courses of lesion effects on LFP coherence between ROI pairs at resting state within the spinal segment below the lesion. Box plots of group-averaged coherences across five specific frequency bands for different horn and intermediate zones pairs: dorsal-to-intermediate zone on lesion side (D-IGM: lesion) (A), dorsal-to-intermediate zone on non-lesion side (D-IGM: non-lesion) (B), dorsal-to-ventral on lesion side (D-V: lesion) (C), and dorsal-to-ventral on non-lesion side (D-V: non-lesion) (D). Control group ($n = 4$ monkeys), 3 months post-injury ($n = 2$), and 6 months post-injury ($n = 7$). Statistical analyses were performed using Brown-Forsythe ANOVA with a Dunnett test or unpaired *t*-test. Significance levels: $^{**}p < 0.005$, $^{***}p < 0.0005$, $^{****}p < 0.0001$.